Chapter 2 A Simple, Clean-Metal Contact Resistance Model

A contact resistance model is presented in this chapter. The model assumes that the contact surfaces are clean, that is, there are no insulating films at the contact interface. The model also assumes that adhesion forces between the contact surfaces are negligible. I first discuss the two broad components of the model - determining the distribution and sizes of the areas in contact at the contact interface, as a function of the contact force; and determining the contact resistance as a function of the distribution and sizes of the areas in contact. Following a description of the model, the predicted contact force – contact resistance characteristics are compared with the measured characteristics of a microswitch.

2.1 Model of Surface Roughness

Determining the nature of the contact area at the interface necessitates a model of the surface roughness of the contact bump and the drain electrode. SEM micrographs of the contact bump surface (Figure 2.1), and SEM micrographs and STM scans of the drain electrode surface indicate that the contact bump is significantly rougher than the drain electrode. The drain electrode is assumed, therefore, to be a flat surface. The problem then becomes to represent the surface of the contact bump.

A large number of researchers have presented work on rough surfaces, particularly in the past three decades. A common approach is one first used in the “asperity-based” model of Greenwood and Williamson [Greenwood 1966]. In the basic GW model, a rough surface

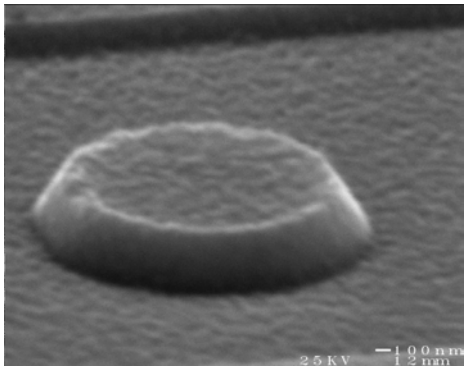

Figure 2.1 *SEM micrograph showing close-up of a contact bump on a microswitch that was flipped over.*

is represented by *asperities* (protuberances) of a prescribed shape and varying heights relative to a reference plane (Figure 2.2). In a general model, both contacting surfaces are rough. However, it has been shown that such a model can be replaced by an equivalent rough surface in contact with a smooth surface [Greenwood 1971]. The asperities are commonly assumed to be spherical, with a certain end radius R, although paraboloid asperities have also been used [Bush 1975]. The distribution of heights is often assumed to be Gaussian, and there is experimental evidence that this is a good assumption for rough surfaces (for example, [Greenwood 1966]). When the surfaces are brought into contact, depending on the separation between the reference planes, the surfaces will be in contact at a certain number of asperities, $i=1,2,...,n$

The deformation of each asperity i results in a circular contact spot of radius a_i. For a given separation between the reference planes, the force on each asperity, F_i, and the radii a_i of the corresponding contact spots can be obtained using an appropriate deformation model, such as the Hertz elastic deformation model [Timoshenko 1951]. Specific

deformation models are discussed in section 1.2. If the asperities are assumed to be sufficiently far apart that they transmit contact forces independently, the total contact force F is the sum of the forces acting on the asperities: $F = \sum_{i=1}^{n} F_i$.

An asperity-based model is not realistic in the sense that it only captures the surface roughness at a particular length scale. Most real surfaces are rough at different length scales (Figure 2.3). For example, SEM micrographs of the contact bump reveal smooth-looking asperities of the order of 0.1 micron (Figure 2.1). However, the SEM used has a resolution of about 0.01 micron, and would probably not be able to reveal roughness on a scale significantly smaller than 0.1 micron. Other researchers have shown that if a surface

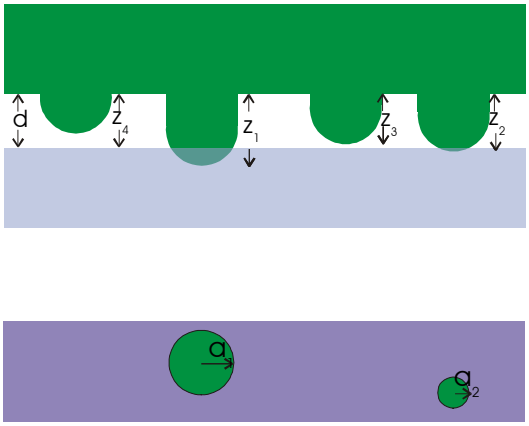

Figure 2.2 *Schematic representation of the Greenwood and Williamson asperity-based model. The rough surface has spherical asperities of radius R, and a certain height distribution. When the rough and smooth surface are in contact, depending on the separation d between the respective reference planes, each contacting asperity is deformed by a certain amount, resulting in the formation of circular contact spots.*

is imaged repeatedly while zooming in, roughness keeps appearing at smaller and smaller scales until atomic steps are visible [Williams 1991]. Some researchers have shown that is possible to capture the surface roughness over multiple length scales using fractal characterization techniques (for example, [Majumdar 1990]).

Fractal models provide a better description of a surface, but are also more complex than asperity-based models. Broadly, a fractal model resembles a set of asperity-based models, each with a different characteristic length. For example, a surface may be assumed to consist of 1 micron radius asperities with a particular roughness (height distribution); the surface of each 1 micron asperity is assumed to have 0.1 micron radius asperities with a different roughness; the surface of each 0.1 micron asperity has 0.01 micron asperities, and so on. In order to capture such information accurately, STM scans of the contact bump surface would be required. I did not pursue this very far because of the logistical difficulties in precisely locating a contact bump under the instrument, and because of the wafer-to-wafer variation in roughness evident in SEM scans.

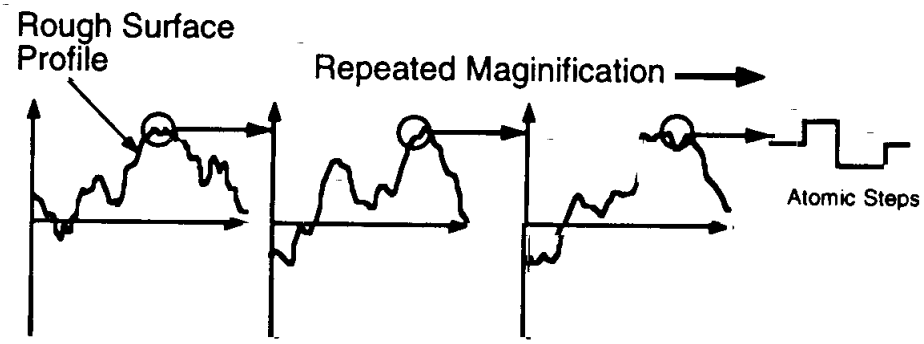

Figure 2.3 *Appearance of a rough surface on successively smaller scales (from [Bhushan 1999])*

However, it is possible to make some simplifying assumptions about the surface roughness. SEM images of the contact surfaces after repeated contact reveal distinct contact spots – where there are indentations as well material transferred between contact surfaces. These are more noticeable on the drain surface because it is much smoother than the contact bump surface. Figure 2.4 shows a typical drain surface after loading to 100 μN, passing a current of 70 mA through the contact, and unloading. The observed spots occur along the arc of a circle, corresponding to the circumference of the contact bump; this is because the surface of the contact bump is slightly cup-shaped, an artifact of the fabrication process. SEM images show that there are typically between 10 and 100 distinct spots; the size of the spots is of the order of 10 nm. This gives us an approximate lower limit of the length scales over which roughness is important. Subsequent modeling will show that an asperity with radius of curvature R=0.01 μm would have to be plastically flattened to a much larger radius in order to yield such a large contact spot. For the asperities corresponding to the contact spots visible in Figure 2.4, an asperity radius of R=0.1 μm represents a reasonable lower limit, at which asperities will not be completely flattened. Originally, there may be significant roughness on smaller length scales, on top of the above asperities. However, since there is evidently significant plastic deformation of the asperities, as evidenced by the material transfer, we should expect roughness on smaller length scales to be smoothed out in the areas of contact.

While developing contact models in this work, model calculations are shown for two different contact bump surfaces, each covered with 100 asperities of radius 0.1 μm; the

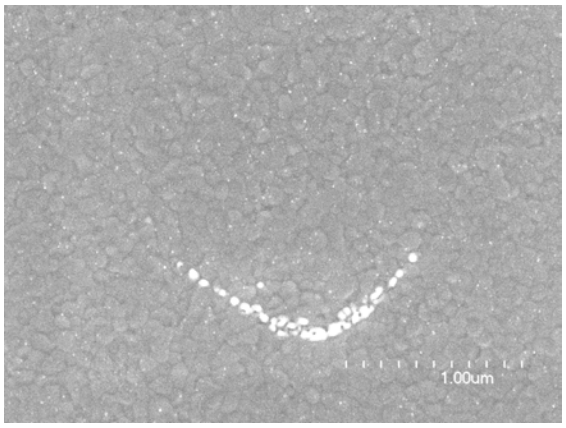

Figure 2.4 *SEM micrograph showing close-up of the drain contact surface on a microswitch that was loaded to a force of 100 μN per contact bump and then unloaded. The scale in the right hand bottom corner shows 10 graduation marks 0.1 μm apart.*

smoother surface has a Gaussian asperity height distribution with standard deviation (σ) = 0.01 μm, and the rougher surface has σ= 0.1 μm. After the final model has been obtained, at the end of Chapter 3, model calculations are shown for a range of asperity radii, and for a range of values of σ; the effects of these parameters on the model results are then discussed.

When a surface with asperities is pressed a certain distance into the flat surface, the load borne by each asperity and the size of the corresponding contact spot has to be determined using an appropriate (elastic or plastic) deformation model. In section 2.2, I discuss the measurement of material properties used in the deformation model. The deformation model for a single asperity is discussed in sections 2.3 and 2.4, followed by a model with multiple asperities of different heights, resulting in multiple contact spots of different sizes (section 2.5).

2.2 Measurement of mechanical properties

The values of hardness and elastic modulus used in the models in this section were obtained from nano-indentation measurements. Samples used for measurements were die from a silicon wafer sputtered with 0.2 μm gold on top of 1 μm SiO_2 at Northeastern University. The measurements were performed at Hysitron Incorporated, Minneapolis. A Berkovich diamond indenter was used to indent the sample to a depth of 8.6 nm. The hardness was defined as the ratio of the maximum load to the projected area. To calculate the modulus of elasticity, a "reduced" modulus, E_r, was calculated from the unloading half-cycle, as $E_r = S\frac{\sqrt{\pi}}{2\sqrt{A}}$, where S is the unloading stiffness $\left(\frac{dP}{dh}\right)$, and A is the projected contact area. From 10 separate measurements, the average values of hardness and reduced modulus were reported as 2.2 GPa and 110 GPa respectively, with standard deviations of 0.1 GPa and 9 GPa respectively.

The reduced modulus is related to the elastic moduli of the sample and the indentor as $\frac{1}{E_r} = \frac{\left(1-\nu_s^2\right)}{E_s} + \frac{\left(1-\nu_i^2\right)}{E_i}$, where the s and i subscripts refer to the sample and indentor respectively. For the indentor, I used the elasticity and Poisson's ratio values supplied by Hysitron, 1140 GPa and 0.07 respectively. The Poisson's ratio of the sample was assumed to be 0.5 – therefore the elastic modulus of the sample can be calculated to be 91 GPa.

The same values of hardness and elastic modulus were used for the other contacting body (the contact bump), since corresponding measured values were not available.

2.3 Contact between sphere and flat

At small contact forces, the deformation of the contacting bodies is elastic, and therefore, fully reversible. Consider the contact between a single spherical asperity of radius *R,* and a flat surface. Let the moduli of elasticity of the contacting bodies be denoted by E_1 and E_2, respectively, and their Poisson's ratios by ν_1 and ν_2 respectively. The effective modulus of elasticity is defined as *K*, where

$$\frac{1}{K} = \frac{3}{4}\left(\frac{1-\nu_1^2}{E_1} + \frac{1-\nu_2^2}{E_2}\right) \tag{2.1}$$

In our case, both contact bodies are assumed to have the same material properties, $E_1=E_2$=91 GPa, and $\nu_1=\nu_2$=0.5. Therefore, $K = \frac{8}{9}E$ =80.9 GPa.

In the absence of any applied contact force, the sphere and the flat touch at a single point (Figure 2.5 (a)). Under an applied contact force *F*, the contacting bodies are pressed against each other, so that corresponding points on the surfaces of the bodies far away from the contact interface approach each other by a distance α. The bodies are brought into contact over a spherical section (Figure 2.5 (b)). The projection of this section on the undeformed flat surface is a circular *contact spot* of radius *a*. The deformation of the contact bodies and the radius of the contact spot are given by the well-known Hertz model. The model is based on the following assumptions:

1. a<<R;

2. there is no friction at the interface;

3. there is no tensile stress in the area of the contact.

Using these assumptions, it can be shown (for example, Johnson(1985), that the radius of the contact spot, *a*, is related to the contact force *F* as

$$a = (\frac{FR}{K})^{1/3} \tag{2.2}$$

The contact radius *a* is related to the vertical deformation α as

$$a = \sqrt{R\alpha} \tag{2.3}$$

As the contact force increases, there is a gradual transition from elastic to plastic deformation over a range of forces. The transition is usually referred to as the elasto-plastic regime. If the von Mises criterion [Timoshenko 1951] is applied to stresses in the

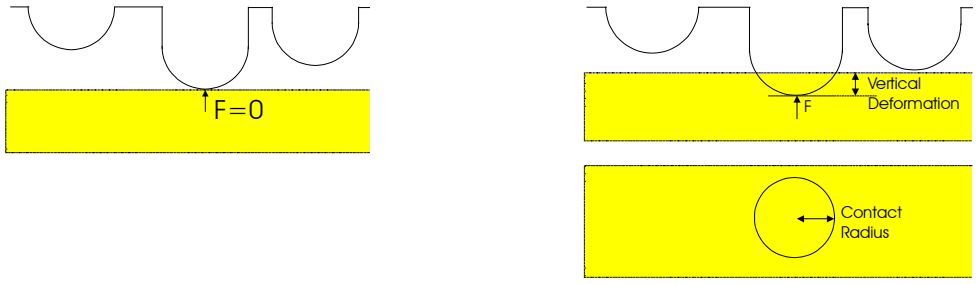

(a) (b)

Figure 2.5 *Schematic representation of contact between a spherical asperity and a flat surface. In the absence of any contact force, contact occurs at a single point (a). Under a force F, the projection of the area of contact on the undeformed flat surface is a circular contact spot (b).*

contact bodies for contact between a sphere and a flat, it is found that the condition for plastic yielding is first reached at a mean contact pressure of $\frac{F}{\pi a^2} = 1.1Y$. The plastic zone is initiated at points within the contacting bodies, on the contact axis and about *0.5a* from the contact interface, where *a* is the contact radius [Timoshenko 1951]. As the contact force increases, the plastic zone expands outwards, in the process reaching the surface and extending over the entire contact area, and the deformation becomes fully plastic. Away from the contact interface, the plastic zone merges into an elastic "hinterland". The elastic deformation produces the counter pressure that balances the contact load, and vanishes when the contact load is removed. When full plasticity is reached, the contact pressure becomes independent of the contact load, and equal to the hardness *H*:

$$p_m = \frac{F}{\pi a^2} = H = 3Y, \tag{2.4}$$

The contact area in the intervening elasto-plastic regime has been given semi-empirically by Studman [Studman 1976] (for ν=0.5):

$$p_m = \frac{F}{\pi a^2} = Y(1 + \frac{2}{3}\ln\frac{Ea}{3YR}), \tag{2.5}$$

Full plasticity is reached (that is, the contact pressure becomes equal to 3*Y*) when $a = a_p \approx 60\frac{RY}{E}$, in agreement with experiments. However, in the Studman model, the transition from elastic to elasto-plastic deformation (when the elastic and elasto-plastic models both give the same contact radius at the same contact force) occurs at $p_m = 0.9Y$, instead of *1.1Y*. Maugis and Pollock (1984) propose a modification of the Studman model, in order to satisfy the von Mises criterion, and still obtain the correct value of a_p at which contact becomes fully plastic. Following this approach, we have:

$$p_m = Y(1.1 + 0.7\ln\frac{Ea}{3.9YR}), \tag{2.6}$$

A simpler, and less physically realistic model is an elastic-perfectly plastic model, with an abrupt transition from the elastic to the plastic. In this case, equation 2.2 is assumed to be valid until the contact pressure becomes equal to the hardness H, at a contact radius $a_p = 3\pi\frac{RY}{K} \approx 11\frac{RY}{E}$, and equation 2.4 holds beyond this point. Figure 2.6 shows the radius of the contact spot as a function of the contact force, using both the modified Studman model and the simple elastic-plastic model. The latter characteristic shows a change in slope at a force of 0.55 μN, corresponding to the elastic-to-plastic transition. The modified Studman model predicts a gradual transition from perfectly elastic deformation up to a force of 0.025 μN to perfectly plastic deformation at a force of 16.3 μN.

The ultimate version of the contact model (including adhesion due to surface forces), developed in Chapter 3, is based on the modified Studman elasto-plastic deformation model. However, in the simpler adhesionless model developed in the rest of this chapter, the simple elastic-perfectly plastic model is used. This is to make it easier to develop a model of subsequent contact, after the contacts have been loaded and unloaded one or more times. This is discussed in greater detail in following sections.

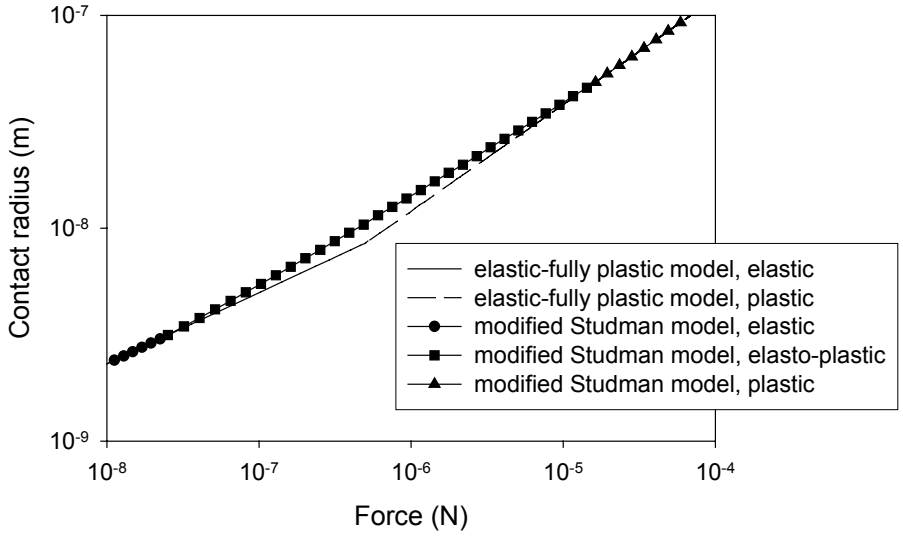

Figure 2.6 *Modeled variation of contact spot radius with load when a single 0.1 micron asperity is pressed into a flat surface, as given by the deformation model of Studman, modified by Maugis and Pollock.*

2.4 Deformation during subsequent contacts

The equations in the previous section describe what happens during contact between an asperity and the flat *for the first time*. The asperities on the contact bump have been assumed to be spherical, with radius R, and the surface of the drain has been assumed to be flat. If the contact force is sufficient to cause some plastic deformation during contact, there is a "flattening" of the asperities, and corresponding concavities are formed in the drain. Upon unloading, the elastic deformation is recovered, but the plastic deformation, persists, so that the asperity now has some radius $R_1<R'$, and the concavity in the drain has a radius $-R_2$, $R_2>R'$.

A simple and commonly accepted assumption is that all of the plastic deformation occurs during the first contact between the sphere and the flat surface. Finite element simulations

of a perfectly plastic deformation model have shown that this is a good assumption in this situation [Kral 1993]. This assumption makes it straightforward to calculate the deformed asperity radius in an elastic-perfectly plastic deformation model. Consider a contact subjected to a contact force F_f, resulting in formation of a contact spot of radius a_f by purely plastic deformation (equation 2.4). Subsequent contacts with a contact force less than or equal to F_f, are governed by the Hertzian solution for elastic contact between a sphere and a concave spherical surface. The Hertz equations for elastic contact between a sphere and a flat are still applicable to this case, if the asperity radius R is replaced by an effective radius R_{eff},

$$\frac{1}{R_{eff}} = \frac{1}{R_1} - \frac{1}{R_2}, \tag{2.7}$$

Re-loading the contact with a force equal to F_f results in elastically forming a contact of the same radius a_f as given by the earlier plastic loading, so that (from the Hertz relation for elastic contact, equation 2.2), the effective radius of curvature is given by:

$$R_{eff} = \frac{Ka_f^3}{F_f}. \tag{2.8}$$

The amount of elastic recovery (α_r) in the height of the asperity during the first unload half-cycle can also be calculated. Since we assume that after the first load-unload cycle, subsequent load-unload cycles are purely elastic and reversible, the elastic recovery must be equal to the vertical deformation when elastically loading to F_f during subsequent cycles. That is,

$$\alpha_r = a_f^2 R_{eff}. \tag{2.9}$$

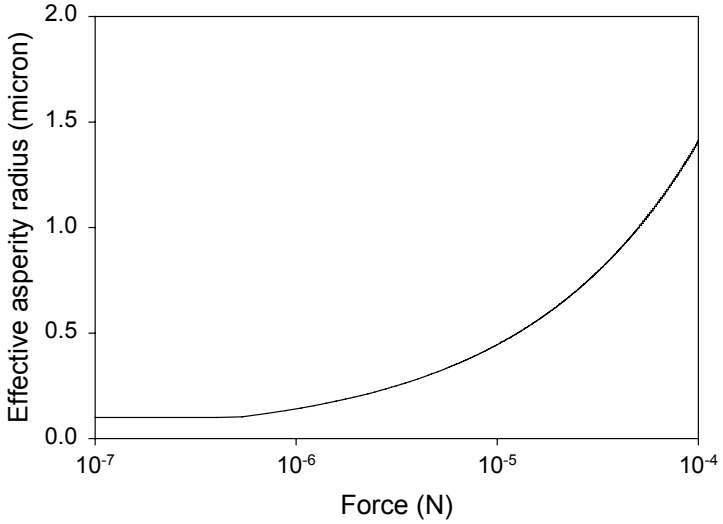

Figure 2.7 *Modeled variation of effective asperity radius R_{eff} as a function of the maximum load on the first cycle. Initial asperity radius is 0.1 micron*

Figure 2.7 shows the calculated variation in R_{eff} with F_f for an asperity with initial radius of curvature, R=0.1 micron. Up to a load of 0.08 μN, the deformation is elastic, and there is no permanent change in the radius of curvature; beyond this load, there is a progressive increase in R_{eff}. Figure 2.8 shows the effect of initial plastic loading up to 20 μN, and 50 μN, on the contact spot radius versus contact force characteristic. Initial loading up to 20 μN results in an effective radius of curvature of 0.63 μm, and the contact radius at that load is 0.054 μm. The characteristic for subsequent loading expectedly shows elastic deformation up to 20 μN, and shows the same contact radius of 0.054 μm at that force. Initial loading up to 50 μN results in R_{eff} =1 μm and a contact radius of 0.085 μm, and similarly shows elastic deformation up to 50 μN on subsequent cycles.

2.5 Multiple asperity model

We now have a model for a how a single asperity deforms under a certain load. Let us consider a model with a distribution of multiple asperities on the surface of the contact bump. Our model is based on a model proposed by Chang, Etsion and Bogy [Chang 1988]. In turn, the CEB model is a refinement of the asperity-based model introduced by Greenwood and Williamson [Greenwood 1966], in which the rough surface is represented by a collection of spherical asperities with identical end radii, whose heights have a statistical distribution. The asperities are assumed to be independent of each other, that is, the load on one asperity does not affect the deformation of another. The area of contact for each asperity in the Greenwood-Williamson model is calculated from the Hertz theory of elastic deformation, even though at a particular contact force the loads on some of the asperities may have exceeded the elastic limit so that the asperities deform plastically. The CEB model calculates the deformation of a plastically deformed asperity on the basis of volume conservation of a certain control volume of the asperity. In the following paragraphs, we briefly explain the equations governing the above model.

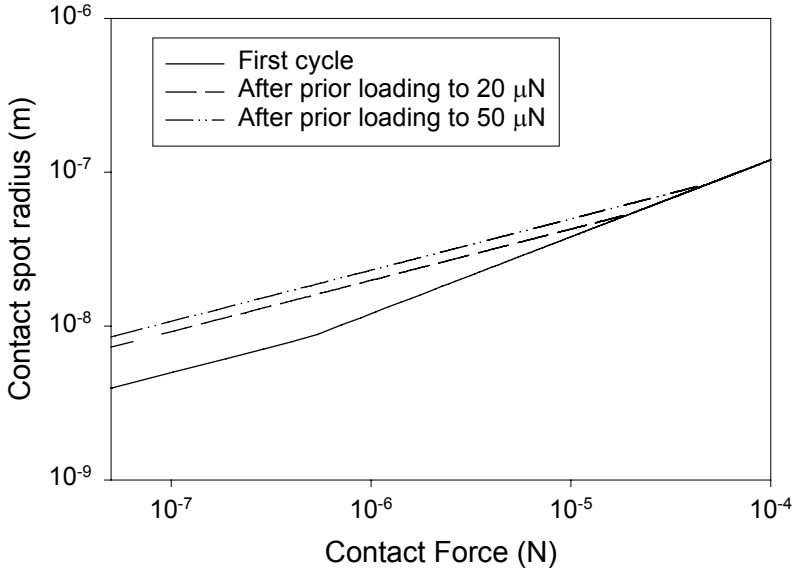

Figure 2.8 *Modeled variation of contact spot radius with load on the first cycle, and on subsequent cycles, after the contact has been previously loaded up to 20 μN and 100 μN respectively. The asperity radius is initially 0.1 micron. The effective asperity radius is 0.61 micron after loading to 20 μN, and 0.95 micron after loading to 50 μN.*

First consider one of the spherical asperities in contact with the flat surface, under a load *F*. Depending on the load, the deformation is either elastic or perfectly plastic. For elastic deformation, the radius of the resulting contact spot is given by Equation 2.2, and the vertical deformation of the asperity is given by Equation 2.3.

Plastic yielding is assumed to occur when the average pressure at the contact interface equals *H,* the hardness of the contacting material. The vertical deformation of the asperity at this transition is given by

$$\alpha_c = (\frac{\pi H}{K})^2 R. \tag{2.10}$$

In the plastic region, the average pressure on an asperity is assumed to be H, so that the contact force on the asperity is

$$F = \pi H a^2. \tag{2.11}$$

In fully plastic deformation, the vertical deformation α is related to the contact radius a as $a = \sqrt{2R\alpha}$, as against $a = \sqrt{R\alpha}$ in elastic deformation. In order to reflect this transition, based on conservation of volume arguments, the vertical deformation is given in the CEB model as:

$$a = \sqrt{R\alpha(2 - \frac{\alpha_c}{\alpha})}, \ \alpha > \alpha_c \tag{2.12}$$

Hence, for a given vertical deformation α, the force on each asperity as well as the radius of the corresponding contact spot can be determined.

Now consider a rough surface with N asperities, each with an end radius of curvature R, and heights $z_1 > z_2 > \ldots > z_N$ (Figure 1.1). Let the separation between the reference planes be d for a given contact force F, such that $z_n > d > z_{n+1}$. Then asperities $1,2,\ldots,n$ come into contact. The vertical deformation of asperity i is given by

$$\alpha_i = z_i - d. \tag{2.13}$$

For a given separation between the reference planes, the force on each asperity, and the radius of each of the corresponding contact spots can be obtained using the previously stated equations.

As mentioned earlier, because of the variability of the roughness of the contact surfaces, contact spot radii are calculated for surfaces with 2 different roughness values - σ = 0.01 μm, and 0.1 μm, where σ is the standard deviation in the asperity heights. Figure 2.9 shows the number of contact spots as a function of the contact force for each of these surfaces (2.9 (a) and 2.9 (c) for σ = 0.01 μm and 0.1 μm respectively) and the variation of a few different asperity contact radii (2.9 (b) and 2.9 (d) respectively). For the smoother surface, 6 asperities are predicted to be in contact at a contact force of 20 μN, increasing to 20 contacting asperities at 100 μN. For the rougher surface, the number of contacting asperities at the above forces is 2 and 3 respectively.

Figure 2.10 shows the same characteristics for two cases – previously unloaded contacts, and contacts that were previously loaded to 100 μN and unloaded. Up to 100 μN, the contact spot radii of the previously loaded contacts vary more gradually with the contact force than the corresponding spot radii of previously unloaded contacts, since the asperities have been flattened by the previous load cycle. At larger forces, the two sets of characteristics are identical.

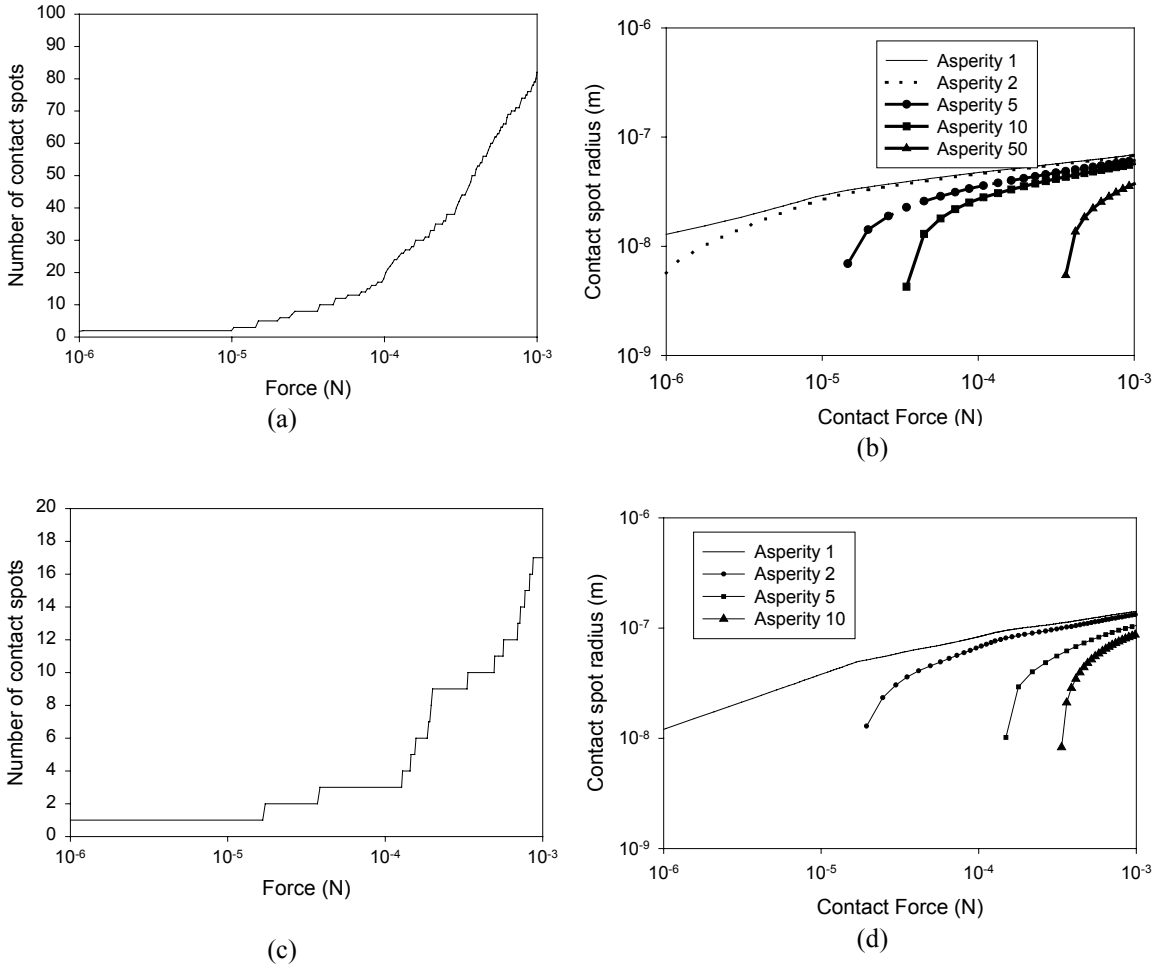

Figure 2.9 *Modeled variation of number of contacting spots, and contact spot radii with contact force for a surface with roughness σ=0.01 micron ((a) & (b)), and σ=0.10 micron ((c) & (d)). The initial asperity radius is 0.1 micron.*

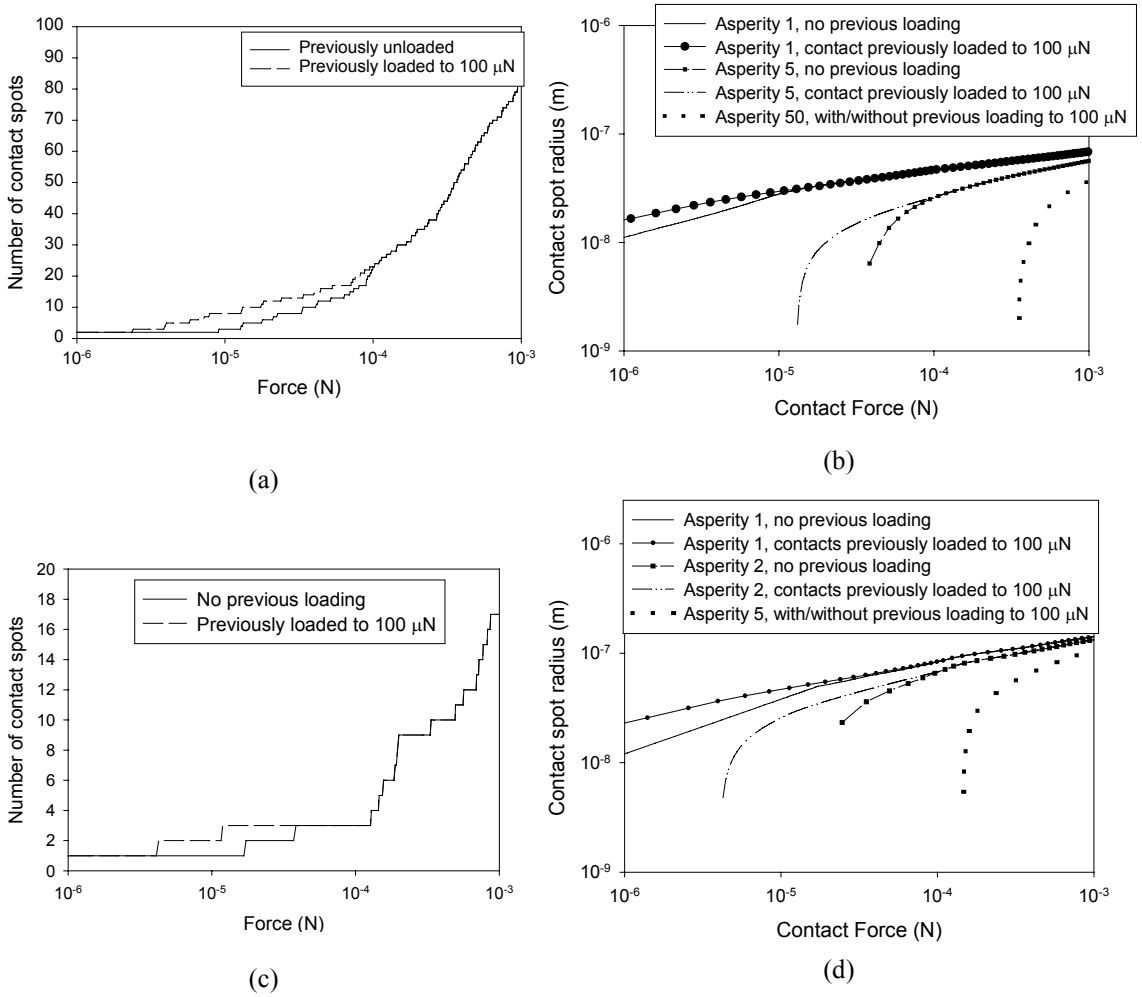

Figure 2.10 *Modeled variation of number of contacting spots, and contact spot radii with contact force, when the contact has previously been loaded to 100 μN and unloaded. Figures 2.10 (a) and 2.10 (b) correspond to a surface with roughness σ=0.01 micron, and 2.10 (c) and 2.10 (d) correspond to a surface with σ=0.10 micron. The same characteristics for a previously unloaded contact (from Figure 2.9) are also shown for comparison.*

2.6 Contact Resistance

The remaining step is to determine the contact resistance, given a certain number of contact spots of known radii. We first consider the contact resistance of a single spot of a

given radius a, separating 2 semi-infinite bodies of resistivity ρ, and then study the more general problem with multiple contact spots of different sizes, and finite contacting bodies. In the single-spot case, the contact resistance arises from two different phenomena. If the radius a is small compared to the electron mean free path length l_e of the material, the resistance of the contact spot is dominated by the Sharvin mechanism [Jansen 1980], in which electrons are projected ballistically through the contact spot without being scattered. In this case,

$$R_{con} = \frac{4\rho l_e}{3\pi a^2} \tag{2.14}$$

On the other hand, if the radius is much larger than the mean free path length, the resistance is dominated a diffuse scattering mechanism, and is given by the Maxwell spreading resistance formula [Holm 1967]:

$$R_{con} = \frac{\rho}{2a} \tag{2.15}$$

Wexler [Wexler 1966] has given a solution of the Boltzmann equation, using the variational principle for resistance of a circular contact spot separating semi-infinite bodies. This results in a simple interpolation formula which can account for the transition between the Maxwell and Sharvin regimes:

$$R_{con} = \frac{4\rho l_e}{3\pi a^2} + \upsilon(l_e / a)\frac{\rho}{2a}. \tag{2.16}$$

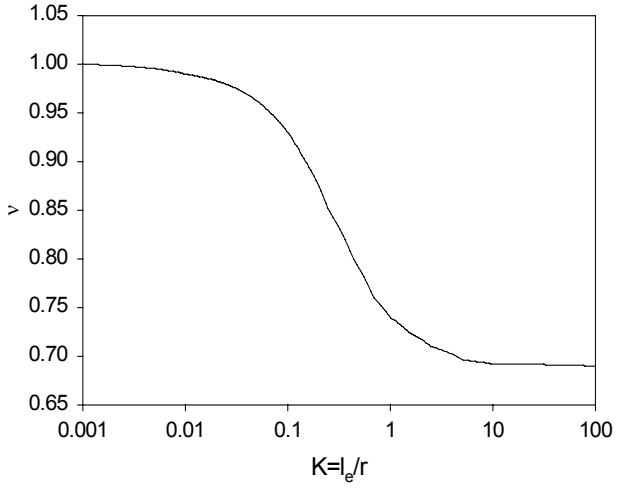

Figure 2.11 *Interpolation factor* ν *to account for transition from Sharvin to Maxwell regime (from Wexler[1966]).*

ν is a slowly varying function of the ratio l_e/a, with $\nu(0)=1$, and $\nu(\infty)=0.694$ (Figure 2.11).

In general, multiple asperities come into contact, resulting in multiple contact spots of varying sizes. The effective contact resistance arising from the contact spots depends on the radii of the spots (given by the contact area model discussed previously) and the distribution of the spots on the contact surface. A lower bound can be obtained on the contact resistance by assuming that contact spots are independent and conduct in parallel (this is equivalent to the exact solution when the radii of the contact spots are small compared to the separation between the spots). Denoting the contact resistance of spot i as $R_{con,i}$,

$$1 / R_{con,lb} = \sum_i 1 / R_{con,i} \qquad (2.17)$$

An upper bound can be obtained on the contact resistance by computing the resistance of a circular spot of radius a_{eff}, and of area equal to the total area of all the individual contact spots combined ($a_{eff} = \sqrt{\sum a_i^2}$).

$$R_{con,ub} = \frac{4\rho l_e}{3\pi a_{eff}^{\ 2}} + \upsilon(l_e / a_{eff})\frac{\rho}{2a_{eff}} \tag{2.18}$$

This upper bound is equivalent to the exact solution when all the conducting spots become large enough to merge into a single conducting spot.

By putting together the contact resistance model given by equations 2.17 and 2.18 with the contact spot radii against force characteristics obtained in section 2.5, we can determine lower and upper bounds on the contact resistance, as a function of the contact force, for a given surface roughness. For model calculations, the resistivity ρ of the drain and beam layers was measured using Van der Pauw structures on the device wafer, as 6.75×10^{-8} Ω-m and 3.85×10^{-8} Ω-m respectively. Since the total contact resistance is the sum of the contact resistances in the two contact bodies, we use the average of the measured resistivity values in equations 2.17 and 2.18. There is some inaccuracy in doing this, since on the underside of the contact bump is a layer of sputtered gold, 0.1 μm thick. The resistivity in this layer is unknown, but probably similar to that in the drain. However, as we will see, there is sufficient uncertainty in calculating the contact resistance that this error is not very important. Figure 2.12(a) shows the calculated dependence of contact resistance on contact force for two surfaces, one with σ=0.1 μm, and the other with σ=0.01 μm. The upper bound characteristic, which depends only on the total contact area, appears to be identical for both surfaces. This is because at low

contact forces, only a single asperity is in contact in either case, and at high forces, all the asperities usually deform plastically, so that the total contact area is the same for both surfaces. Figure 2.12(b) shows the calculations for switch contacts which were previously loaded to 100 μN and unloaded, and deformation is consequently purely elastic. In this case, too, the upper bound characteristic is independent of the surface roughness - although there is no longer any plastic deformation, the contact area is determined by the previous plastic deformation.

2.7 Effect of finite contact geometry

The contact resistance expressions of equations 2.17 and 2.18 are based on an ideal contact geometry – a circular contact spot separating two semi-infinite contacting bodies. One of the contacting bodies in the microswitch is the drain electrode. Since the drain thickness – 0.2 micron – is comparable to the contact area, the semi-infinite idealization does not appear to hold. To determine the error caused by making the semi-infinite assumption, the contact geometry of Figure 2.13 was simulated, by a finite element solution of the Maxwell model. For a contact spot radius a=0.1 micron, the Maxwell contact resistance is $R_{con} = \frac{\rho}{2a}$. The finite element simulation gives $R_{con} = 1.07\frac{\rho}{2a}$.

The error introduced by the assumption in the Sharvin model was not evaluated.

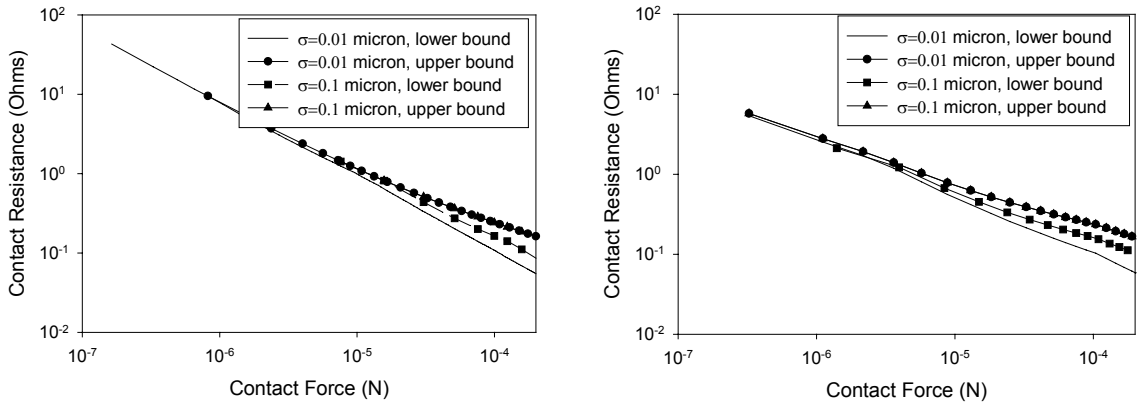

Figure 2.12 *Modeled contact resistance vs contact force characteristics, on the first cycle (a), and after the switch has previously loaded to 100* μ*N and unloaded (b). In each graph, the upper bounds for the two values of* σ *nearly coincide.*

1.8 Measured contact resistance

Contact resistance was measured using a microswitch design with an extra pair of terminals which allow the voltage across the contact to be measured (Figure 2.14). Figure 2.15 shows the contact resistance of a microswitch, measured as a function of the gate-to-source actuation voltage. For a previously untested microswitch, the contact resistance is 0.5 Ω - 1 Ω for actuation voltages up to 90 V, and decreases gradually as the actuation voltage is increased. As the switch is cycled by turning it on and off repeatedly, its contact resistance decreases. The switch in Figure 2.15 has a contact resistance of the order of 0.1 Ω. after 1000 test cycles. However, it now also varies less with the actuation voltage than before.

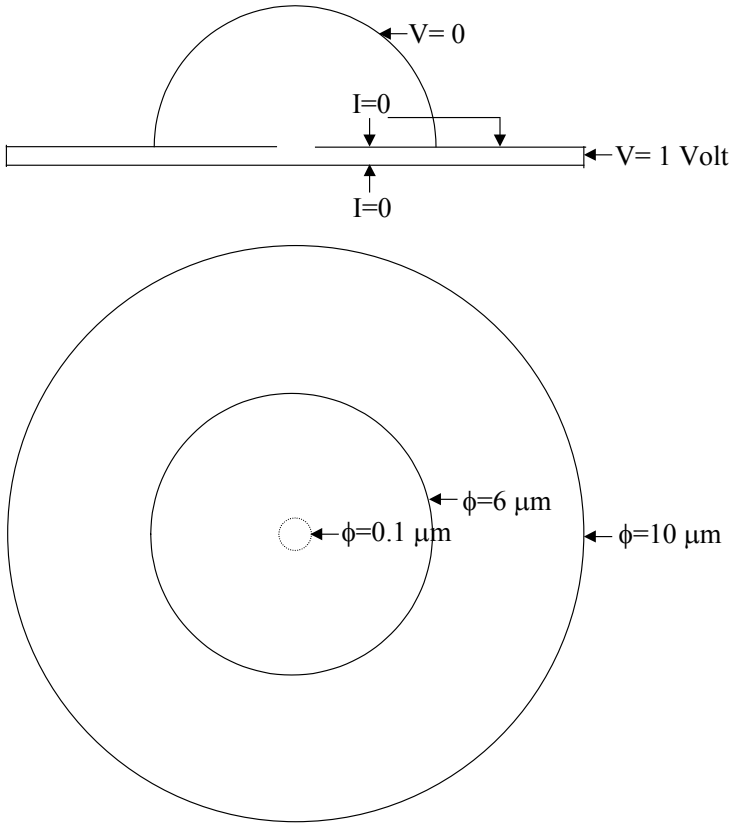

Figure 2.13 Contact model used to study deviation from ideal constriction. The upper hemisphere represents the beam, and the lower cylinder represents the drain electrode. The dotted-line circle is a contact spot at their interface, diameter 0.1 micron.

In order to compare the measured contact resistance with the contact resistance model, it is necessary to map the actuation voltage to the contact force. This can be done by modeling the microswitch as a beam which is clamped at its fixed end, and simply supported at its free end (Figure 2.16). The Euler-Bernoulli beam equations are used to determine the beam deflection and contact force boundary condition, assuming a certain distributed electrostatic force acting on the beam. In turn, the new electrostatic force is determined as a function of the beam shape. The two steps are repeated iteratively, until

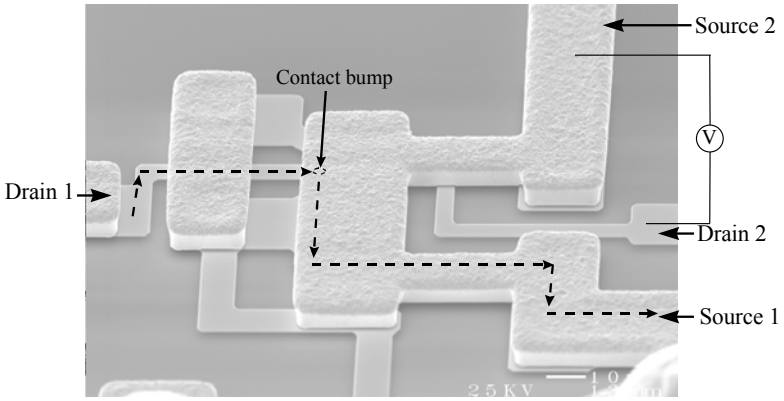

Figure 2.14 Microswitch geometry used to measure contact resistance. Current (represented by the broken lines) is forced between one pair of source and drain terminals, and the other pair of source and drain terminals is used to measure the voltage across the contact. The contact bump on the lower surface of the beam is not visible in this micrograph.

the solution converges. Figure 2.17 shows the modeled variation of contact force with gate voltage for the microswitch shown in Figure 2.14. An actuation voltage of 90 V is seen to correspond to a contact force of approximately 100 μN.

Using this model, the measured contact resistance characteristics of Figure 2.15 are plotted as a function of contact force in Figures 2.18 (a) and (b). The lower and upper bounds predicted by the contact resistance model for a previously uncycled switch are shown for comparison in Figure 2.18 (a), and the contact resistance bounds for a switch previously subjected to a 100 μN load are shown in Figure 2.18 (b). The initial measured resistance is 0.3-0.6 Ω higher than predicted, and its dependence on contact force has roughly the same shape as predicted. The measured resistance after 1000 switch cycles is much less sensitive to the contact force than predicted by the model, and correspondingly, much lower than predicted at low contact forces.

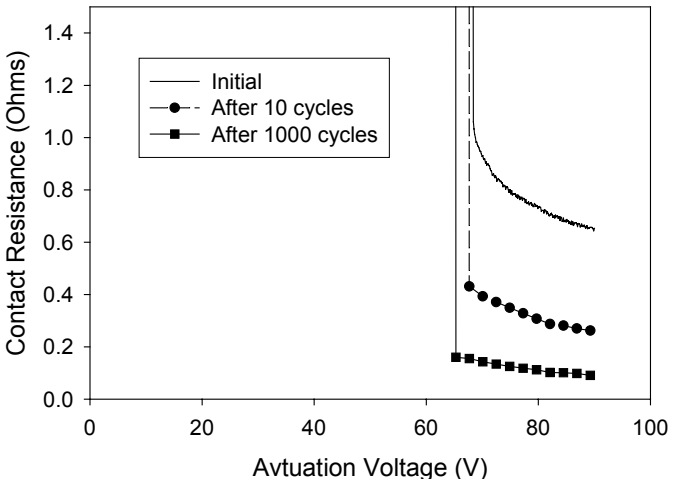

Figure 2.15 Measured contact resistance as a function of actuation voltage, for a previously untested switch, and after the same switch had been cycled 10 times and 1000 times with an actuation voltage of 78 V and a current of 4 mA.

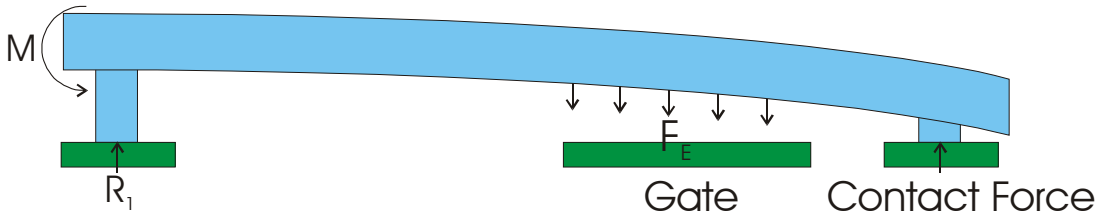

Figure 2.16 Beam model of microswitch in closed position. The fixed end of the beam is assumed to be clamped, and the contact bump is assumed to be simply supported at the drain.

It seems reasonable to assume that the lower contact resistance after cycling the switch is a result of repeated "scrubbing" of the contact surfaces resulting in a cleaner contact interface. However, this does not explain the reduced sensitivity to the contact force. The reason for this phenomenon appears to be adhesion between the contact surfaces. If there is significant adhesion between the contact surfaces, this would tend to hold them closed while the contacts are being unloaded, reducing the sensitivity of the contact resistance to the contact force. It would also result in a hysteresis - the switch would open at a smaller actuation voltage than that at which it closes. This is indeed observed in measurements – Figure 2.19 shows the measured contact resistance of a switch when the actuation voltage is increased from 0 to 90 V, and then decreased back

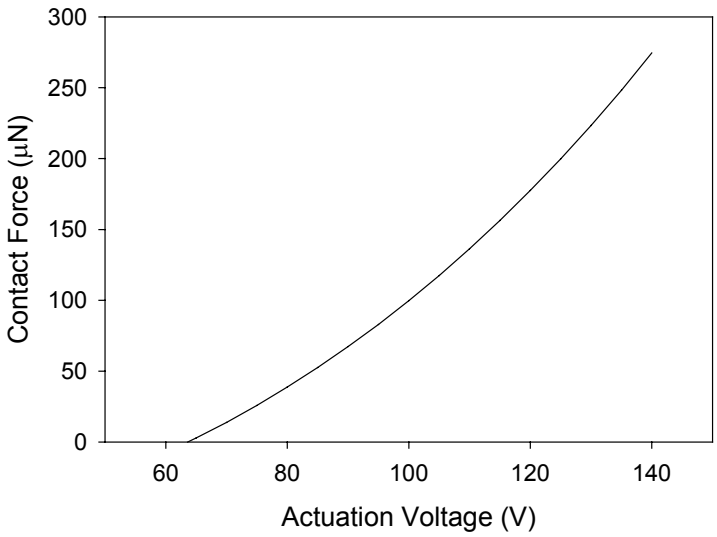

Figure 2.17 Modeled variation of contact force with gate-to-source actuation voltage for the microswitch geometry of Figure 1.5.

to 0 (this is actually the same measurement as shown in Figure 2.18 (b) – only the loading half-cycle was shown in Figure 2.18 (b)). The switch closes at 65 V, and opens at 45 V.

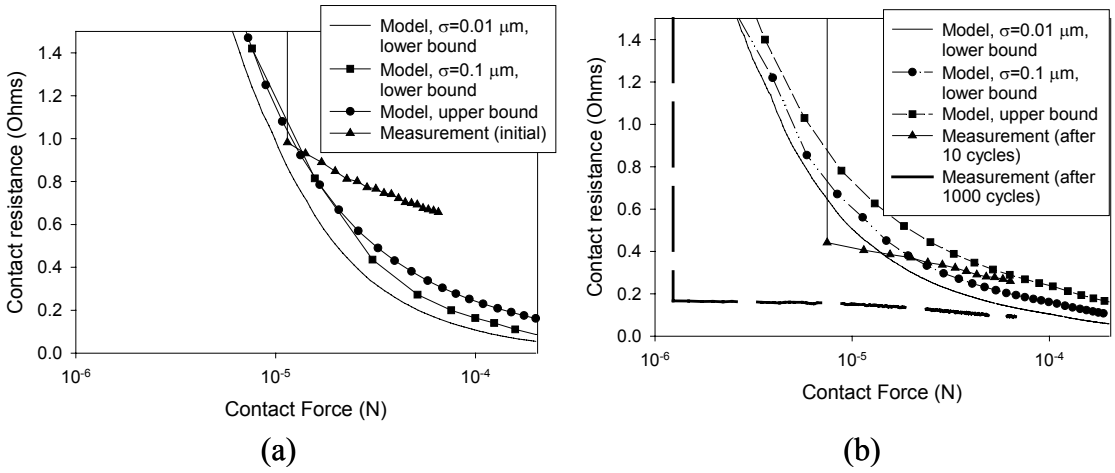

Figure 2.18 Comparison of measured contact resistance with the contact resistance model. The measured characteristics are the ones shown in Figure 2.15: 2.18(a) shows the measured resistance of a previously untested switch, and (b) shows the measured resistance after 1000 switch cycles. The modeled contact resistance for a previously untested switch is shown for comparison in 2.18(a), and the modeled contact resistance for a contact previously subjected to 100 μN is shown in (b).

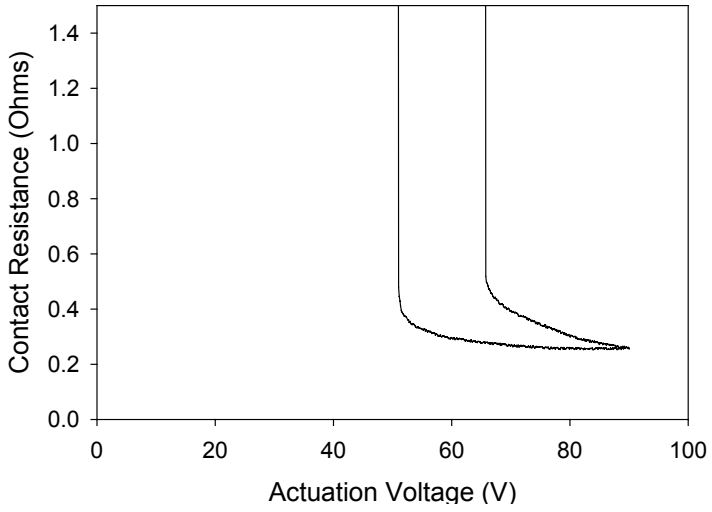

Figure 2.19 Hysteresis in contact resistance measurements. Contact resistance was measured first while the actuation voltage was increased from 0 to 90 V, and then while it was decreased back to 0.

Apart from contact adhesion, another possible reason for the observed hysteresis is the well-known mechanical instability of electrostatically actuated structures. This results in a pull-in of the beam at some critical beam-gate, which is different in the open and closed positions of the switch. However, the Euler-Bernulli beam model predicts that there is little or no hysteresis in the switch arising from mechanical instability. Also, the amount of hysteresis is found to change as a switch is cycled. There is also a strong correlation between the contact resistance and the actuation voltage at which the switch opens, indicating that a cleaner contact results in more hysteresis (Figure 2.20).

Clearly, a major element missing from the contact resistance model at this stage is contact adhesion. In Chapter 3, I will present a contact resistance model that includes contact force, and study different aspects of contact adhesion and the resulting hysteresis.

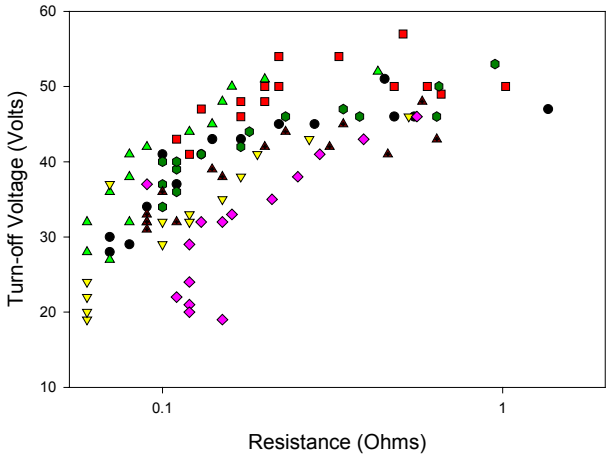

Figure 2.20 *Measured turn-off voltage of a group of 7 microswitches; each device was cycled 10^6 times, and its contact resistance and turn-off voltage was measured at intervals while cycling. The measured turn-off voltage is plotted as a function of contact resistance.*

References

[Greenwood 1966] J. A. Greenwood and J.B.P. Williamson, "Contact of Nominally Flat Surfaces", *Proceedings of the Royal Society (London)*, Vol. 295, pp. 300-319, 1966.

[Greenwood 1971] J. A. Greenwood and J. H. Tripp, "The Contact of Two Nominally Flat Rough Surfaces", *Proceedings of Institution of Mechanical Engineers*, Vol. 185, 625-633.

[Bush 1975] A. W. Bush, R. D. Gibson and T. R. Thomas, "The Elastic Contact of a Rough Surface", *Wear*, Vol. 35, pp. 87-111, 1975.

[Timoshenko 1951] S. Timoshenko and J. Goodier, Theory of Elasticity, McGraw Hill (New York), 2nd ed., 1951.

[Bhushan 1998] B. Bhushan (ed.), Handbook of Micro/Nanotribology, CRC Press (Boca Raton), 2nd ed., 1998.

[Williams 1991] E. D. Williams and N. C. Bartlett, "Thermodynamics of Surface Morphology", *Science*, Vol. 251, pp. 393-400, 1991.

[Majumdar 1990] A. Majumdar and B. Bhushan, "Role of Fractal Geometry in Roughness Characterization and Contact Mechanics of Surfaces", *ASME Journal of Tribology*, Vol. 112, pp. 205-216, 1990.

[Studman 1976] C. J. Studman, M. A. Moore and S. E. Jones, *Journal of Physics D, Applied Physics*, Vol. **10,** pp. 949-958, 1976.

[Kral 1993] E. R. Kral, K. Komvopoulos, and D. B. Bogy, "Elastic-Plastic Finite Element Analysis of Repeated Indentation of a Half-Space by a Rigid Sphere", *Journal of Applied Mechanics*, Vol. 60, pp. 829-841, 1993.

[Chang 1988] W. R. Chang, I. Etsion, and D.B. Bogy, "An Elastic-Plastic Model for the Contact of Rough Surfaces", *Journal of Tribology*, Vol. 109, pp. 257-263, 1988.

[Jansen 1980] A. G. M. Jansen, A. P. van Gelder, and P. Wyder, "Point-Contact Spectroscopy in Metals", *Journal of Physics*, Vol. C13, pp. 6073-6118, 1980.

[Holm 1967] R. Holm, Electric Contacts, Springer-Verlac (New York), 1967.

[Wexler 1966] G. Wexler, "The Size Effect and the Non-Local Boltzmann Transport Equation in Orifice and Disk Geometry", *Proceedings of Physical Society*, Vol. 89, pp. 927-941, 1966.

[Johnson 1985] K. L. Johnson, Contact Mechanics, Cambridge University Press, Cambridge, MA, 1985.